REVISTA MATÉRIA V.31
ISSN 1517-7076 articles e20260102, 2026

ZIF-67-Derived Co_3O_4/N-Doped carbon nanocomposites for sensitive electrochemical determination of nitrite in water

Wei Song[1], An Lu[2]*

[1]Nanyang Institute of Technology, School of Biological and Chemistry. 473004, Nanyang, Henan, China.
[2]Chongqing Academy of Metrology and Quality Inspection. Chongqing, 401120, China.
e-mail: song78wei@163.com, anwonderwonder56@163.com

ABSTRACT

The escalating issue of nitrite (NO_2^-) contamination in aquatic environments necessitates the development of highly sensitive and selective detection methods. In this study, a series of porous Co_3O_4/N-doped carbon (Co_3O_4/NC) nanocomposites were successfully synthesized through a facile one-step pyrolysis of a zeolitic imidazolate framework-67 (ZIF-67) precursor at varying temperatures (500, 600, 700, and 800 °C). The effect of pyrolysis temperature on the physicochemical properties and electrochemical sensing performance of the resulting materials was systematically investigated. The optimized nanocomposite, Co_3O_4/NC-700, obtained at 700 °C, exhibited a well-defined porous dodecahedral morphology with uniformly dispersed Co_3O_4 nanoparticles embedded within a highly conductive N-doped carbon matrix. This unique architecture provided a large electroactive surface area, abundant active sites, and rapid electron transfer pathways. When employed as an electrode modifying material for electrochemical nitrite sensing, the Co_3O_4/NC-700 based sensor demonstrated outstanding performance, including a wide linear range from 0.1 μM to 1500 μM, a high sensitivity of 850.3 μA mM^{-1} cm^{-2}, and an ultralow detection limit of 0.03 μM (S/N = 3). Furthermore, the sensor exhibited good repeatability (RSD = 2.8%, n = 7), electrode-to-electrode reproducibility (RSD = 3.9%, n = 5), and retained 94.5% of its initial response after 30 days. In tap water and river water, recoveries obtained by the standard addition method ranged from 98.6% to 103.2%, confirming the reliability of the proposed sensor for real-sample analysis. This work presents a simple and effective strategy for designing advanced MOF-derived nanocomposites for high-performance environmental monitoring applications.

Keywords: MOF-derived materials; Porous polyhedral architecture; Heteroatom-modified carbon matrix; Non-enzymatic sensing; Environmental contaminant monitoring.

1. INTRODUCTION

Nitrite (NO_2^-), an intermediate species in the nitrogen cycle, has become a significant environmental pollutant due to its widespread use in industrial processes, food preservation, and as an agricultural fertilizer [1, 2]. The excessive discharge of nitrite-containing wastewater into aquatic ecosystems poses a severe threat to both environmental balance and human health. When ingested, nitrite can lead to methemoglobinemia, a condition that impairs the oxygen-carrying capacity of blood, and can also react with amines in the human body to form carcinogenic N-nitrosamines [3]. Consequently, the World Health Organization (WHO) and the U.S. Environmental Protection Agency (EPA) have established stringent maximum allowable limits for nitrite in drinking water, typically around 3 mg L^{-1} (approximately 65.2 μM) [4]. Therefore, the development of rapid, sensitive, and reliable methods for the quantitative determination of nitrite is of paramount importance for public health and environmental protection.

Conventional methods for nitrite analysis, such as spectrophotometry, chromatography, and fluorescence, while accurate, often suffer from several drawbacks, including time-consuming procedures, the need for sophisticated instrumentation, complex sample pretreatment, and high operational costs [5]. These limitations restrict their applicability for on-site and real-time monitoring. In contrast, electrochemical sensing techniques have emerged as a highly attractive alternative owing to their inherent advantages of simplicity, rapid response, low cost, portability, high sensitivity, and excellent selectivity [6]. The core of an electrochemical sensor lies in the electrode material, whose properties directly govern the overall sensing performance. Therefore, extensive

Corresponding Author: An Lu Received on 04/02/2026 Accepted on 16/03/2026

DOI: https://doi.org/10.1590/1517-7076-RMAT-2026-0102

research has been devoted to the design and synthesis of advanced nanomaterials to construct high-performance electrochemical sensors for nitrite.

Among various candidate materials, transition metal oxides have garnered considerable attention for electrocatalytic applications due to their multiple oxidation states, high stability, and natural abundance. In particular, cobalt oxide (Co_3O_4) is considered a promising electrocatalyst for nitrite oxidation due to its excellent catalytic activity, low cost, and environmental benignity [7, 8]. However, the practical application of pure Co_3O_4 nanomaterials is often hindered by their intrinsic poor electrical conductivity and tendency to agglomerate, which limits the accessibility of active sites and reduces electrocatalytic efficiency [9, 10]. To overcome these issues, a common strategy is to integrate Co_3O_4 nanoparticles with conductive carbon-based supports, such as graphene, carbon nanotubes, or porous carbon. Nitrogen-doped carbon (NC) is an especially effective support material because nitrogen doping can modulate the electronic structure of the carbon matrix, create defect sites, improve wettability, and generate additional active centers, thereby significantly enhancing the overall electrocatalytic performance [11, 12]. Recent studies on pollutant sensing have shown that analytical performance is strongly governed by the architecture of the active material and the transduction mode employed. Electrochemical platforms remain particularly attractive for water-quality monitoring because they combine rapid response, low instrumentation cost, and on-site applicability [13–16]. Recent reviews have emphasized that for nitrite sensing, improved performance is commonly achieved by coupling catalytically active metal oxides with conductive carbonaceous supports or defect-engineered nanostructures. In parallel, MOF-derived and ZIF-based materials have emerged as versatile candidates because they provide controlled porosity, high surface area, and compositional tunability. For example, a recent Ionics study reported a ZIF-67@g-C_3N_4 colorimetric nitrite sensor with excellent sensitivity, illustrating the broader potential of ZIF-derived architectures; however, optical/colorimetric systems and electrochemical systems differ substantially in instrumentation, operational simplicity, and electrode interfacial kinetics. Therefore, the development of a robust electrochemical nitrite sensor based on a MOF-derived conductive porous framework remains highly relevant.

Metal-Organic Frameworks (MOFs), a class of crystalline porous materials constructed from metal ions or clusters coordinated to organic linkers, have been recognized as ideal precursors or self-sacrificial templates for synthesizing various functional nanomaterials [17, 18]. Their exceptionally high surface areas, tunable porosity, and uniform distribution of metal and organic components at the molecular level make them uniquely suited for this purpose. Zeolitic imidazolate framework-67 (ZIF-67), composed of Co^{2+} nodes and 2-methylimidazole linkers, was selected in this work because it offers several advantages over the direct synthesis of bare Co_3O_4. First, ZIF-67 acts simultaneously as a cobalt source, a nitrogen-containing carbon precursor, and a self-sacrificial polyhedral template [19, 20]. During pyrolysis, the organic linker is carbonized in situ to form an N-doped conductive carbon matrix, while cobalt species are converted into finely dispersed Co_3O_4 nanocrystallites. This route therefore enables intimate interfacial coupling between Co_3O_4 and N-doped carbon, suppresses nanoparticle agglomeration, and preserves a porous polyhedral framework with a high density of accessible active sites [21, 22]. In contrast, directly prepared Co_3O_4 commonly suffers from lower conductivity, broader particle-size distribution, and less controlled porosity, all of which are unfavorable for rapid electron transfer and efficient mass transport. For electrochemical nitrite sensing, the ZIF-67-derived route is therefore advantageous because it integrates catalytic Co_3O_4 sites with a conductive and defect-rich carbon network in a single material.

The properties of MOF-derived materials are highly dependent on the synthesis conditions, with the pyrolysis temperature being one of the most critical parameters [23, 24]. The temperature influences the degree of carbonization, the phase of the resulting cobalt species (metallic Co, CoO, or Co_3O_4), the nitrogen content and speciation, the porosity, and the overall morphology of the final product [25–27]. By carefully tuning the pyrolysis temperature, it is possible to optimize the material's structure and composition to achieve superior electrochemical performance. For instance, an appropriate temperature can ensure the complete decomposition of the organic linker to form a graphitic carbon network while converting Co^{2+} to catalytically active Co_3O_4, preserving a porous structure inherited from the ZIF-67 precursor [28].

In this work, we report a systematic study on the synthesis of ZIF-67-derived Co_3O_4/N-doped carbon (Co_3O_4/NC) nanocomposites via a simple one-step pyrolysis method. By varying the pyrolysis temperature from 500 °C to 800 °C, we fabricated a series of materials (denoted as Co_3O_4/NC-T, where T is the temperature) and thoroughly investigated the influence of this parameter on their morphology, structure, composition, and ultimately, their electrocatalytic activity towards nitrite oxidation. The synthesized materials were extensively characterized using a suite of analytical techniques. The electrochemical performance of the composites as sensors for nitrite was evaluated using cyclic voltammetry and amperometry. The nanocomposite prepared at 700 °C (Co_3O_4/NC-700) demonstrated the most favorable combination of properties, leading to an electrochemical sensor with exceptional sensitivity, a low limit of detection, a wide linear response range, and excellent long-term stability for nitrite determination in water.

2. MATERIALS AND METHODS

2.1. Chemicals and reagents

Cobalt(II) nitrate hexahydrate ($Co(NO_3)_2 \cdot 6H_2O$, ≥99.0%) and 2-methylimidazole ($C_4H_6N_2$, 99%) were purchased from Sigma-Aldrich. Methanol (CH_3OH, ≥99.8%), ethanol (C_2H_5OH, ≥99.5%), and Nafion solution (5 wt%) were obtained from Alfa Aesar. Sodium nitrite ($NaNO_2$), potassium chloride (KCl), sodium chloride (NaCl), sodium nitrate ($NaNO_3$), potassium sulfate (K_2SO_4), glucose, uric acid, and ascorbic acid were supplied by Merck. Phosphate buffer solution (PBS, 0.1 M) was prepared by mixing stock solutions of NaH_2PO_4 and Na_2HPO_4, and the pH was adjusted using 0.1 M H_3PO_4 or NaOH. All aqueous solutions were prepared with deionized (DI) water (18.2 MΩ·cm) obtained from a Millipore Milli-Q system. All chemicals were of analytical grade and used as received without further purification.

2.2. Synthesis of ZIF-67 precursor

The ZIF-67 precursor was synthesized using a previously reported precipitation method with slight modifications [29, 30]. In a typical synthesis, 2.91 g (10 mmol) of $Co(NO_3)_2 \cdot 6H_2O$ was dissolved in 100 mL of methanol in a beaker to form a clear pink solution, designated as solution A. In a separate beaker, 6.56 g (80 mmol) of 2-methylimidazole was dissolved in 100 mL of methanol to form solution B. Subsequently, solution A was rapidly poured into solution B under vigorous magnetic stirring. The mixture immediately turned into a purple suspension. The stirring was continued for 24 hours at room temperature (25 °C) to allow for complete crystal growth. The resulting purple precipitate was collected by centrifugation at 8000 rpm for 10 minutes, washed thoroughly with fresh methanol three times to remove any unreacted reagents, and finally dried in a vacuum oven at 60 °C for 12 hours.

2.3. Synthesis of Co_3O_4/NC nanocomposites

The Co_3O_4/N-doped carbon (Co_3O_4/NC) nanocomposites were prepared via a one-step thermal decomposition of the as-synthesized ZIF-67 precursor [31]. A certain amount of the dried ZIF-67 powder was placed in a ceramic boat and positioned in the center of a horizontal tube furnace. The furnace was first purged with high-purity nitrogen (N_2) gas for 30 minutes to create an inert atmosphere. Then, the furnace was heated to a target temperature of 500 °C, 600 °C, 700 °C, or 800 °C at a heating rate of 5 °C/min and held at that temperature for 2 hours under a continuous N_2 flow. After the pyrolysis process, the furnace was allowed to cool naturally to room temperature. The obtained black powder samples were collected and designated as Co_3O_4/NC-500, Co_3O_4/NC-600, Co_3O_4/NC-700, and Co_3O_4/NC-800, corresponding to the pyrolysis temperatures used.

2.4. Material characterization

The morphology and microstructure of the synthesized materials were examined using field-emission scanning electron microscopy (JSM-7600F, JEOL, Tokyo, Japan) equipped with an energy-dispersive X-ray spectroscopy (EDS) detector for elemental analysis and mapping. Further morphological details and lattice structures were investigated by transmission electron microscopy (TEM) and high-resolution TEM (HRTEM) on a JEOL JEM-2100F (JEM-2100F, JEOL, Tokyo, Japan) instrument operating at 200 kV. The crystal structure and phase composition of the samples were determined by X-ray diffraction (XRD) using a Bruker D8 Advance diffractometer with Cu Kα radiation (λ = 1.5406 Å) over a 2θ range of 5° to 80°. Thermogravimetric analysis (TGA, Q500, TA Instruments, New Castle, DE, USA) was performed on a TA Instruments Q500 analyzer from room temperature to 900 °C at a heating rate of 10 °C/min under a nitrogen atmosphere to study the thermal stability of the ZIF-67 precursor. Raman spectra (inVia, Renishaw, Gloucestershire, UK) were recorded on a Renishaw inVia Raman microscope with a 532 nm laser excitation source. Nitrogen adsorption-desorption isotherms were measured at 77 K using a Micromeritics ASAP 2020 analyzer (ASAP 2020, Micromeritics, Norcross, GA, USA). The specific surface area was calculated using the Brunauer-Emmett-Teller (BET) method, and the pore size distribution was derived from the desorption branch of the isotherm using the Barrett-Joyner-Halenda (BJH) model [32]. The surface chemical composition and elemental valence states were analyzed by X-ray photoelectron spectroscopy (XPS, K-Alpha$^+$, Thermo Fisher Scientific, East Grinstead, UK) on a Thermo Fisher Scientific K-Alpha$^+$ spectrometer with a monochromatic Al Kα X-ray source.

2.5. Electrochemical measurements

To prepare the working electrode, 2.0 mg of the synthesized Co_3O_4/NC catalyst was dispersed in a 1.0 mL solution containing 950 μL of ethanol and 50 μL of 5 wt% Nafion solution. The mixture was ultrasonicated for 30 minutes to form a homogeneous black ink. Before modification, the bare GCE was polished sequentially with 1.0, 0.3, and 0.05 μm alumina slurries on a polishing cloth, followed by ultrasonication in ethanol and DI

water, and finally dried under a nitrogen stream. Then, 5.0 μL of the catalyst ink was carefully drop-cast onto the pre-cleaned GCE surface and allowed to dry naturally at room temperature to form the Co_3O_4/NC/GCE modified electrode.

Cyclic voltammetry (CV) was conducted in 0.1 M PBS (pH 7.0) within a potential window of 0.0 V to +1.2 V. Electrochemical impedance spectroscopy (EIS) was performed in a solution of 5.0 mM $[Fe(CN)_6]^{3-/4-}$ containing 0.1 M KCl over a frequency range from 100 kHz to 0.1 Hz with an AC amplitude of 5 mV. Amperometric (i-t) measurements for nitrite detection were carried out in stirred 0.1 M PBS (pH 7.0) at a constant applied potential of +0.80 V. For LOD evaluation, the blank response was recorded repeatedly under the same conditions, and the detection limit was calculated using the 3σ/S criterion from the blank standard deviation and the slope of the calibration curve. For real-sample analysis, nitrite was quantified by the standard addition method. For selectivity tests, the amperometric response to 100 μM nitrite was recorded after the addition of various interfering species.

To optimize the amperometric conditions, the effects of solution pH (6.0–8.0) and applied potential (+0.60 to +0.90 V vs. Ag/AgCl) were evaluated using 100 μM nitrite. The highest signal-to-background ratio was obtained in 0.1 M PBS at pH 7.0 and +0.80 V; therefore, these conditions were used for all subsequent measurements.

3. RESULTS AND DISCUSSION

3.1. Synthesis and morphological characterization

The synthetic strategy for the Co_3O_4/NC nanocomposites is illustrated by the controlled pyrolysis of a ZIF-67 precursor. Initially, ZIF-67 crystals were synthesized through a simple co-precipitation reaction between Co^{2+} ions and 2-methylimidazole linkers in methanol at room temperature. The scanning electron microscopy (SEM) image of the as-prepared ZIF-67 precursor is shown in Figure 1. The image reveals that the precursor consists of uniform polyhedral crystals with a well-defined rhombic dodecahedral morphology, which is the characteristic shape of ZIF-67 [33, 34]. The crystals exhibit smooth surfaces and sharp edges, with an average particle size of approximately 650 ± 50 nm. This uniform morphology and size distribution make ZIF-67 an ideal template for deriving porous carbon-based nanomaterials.

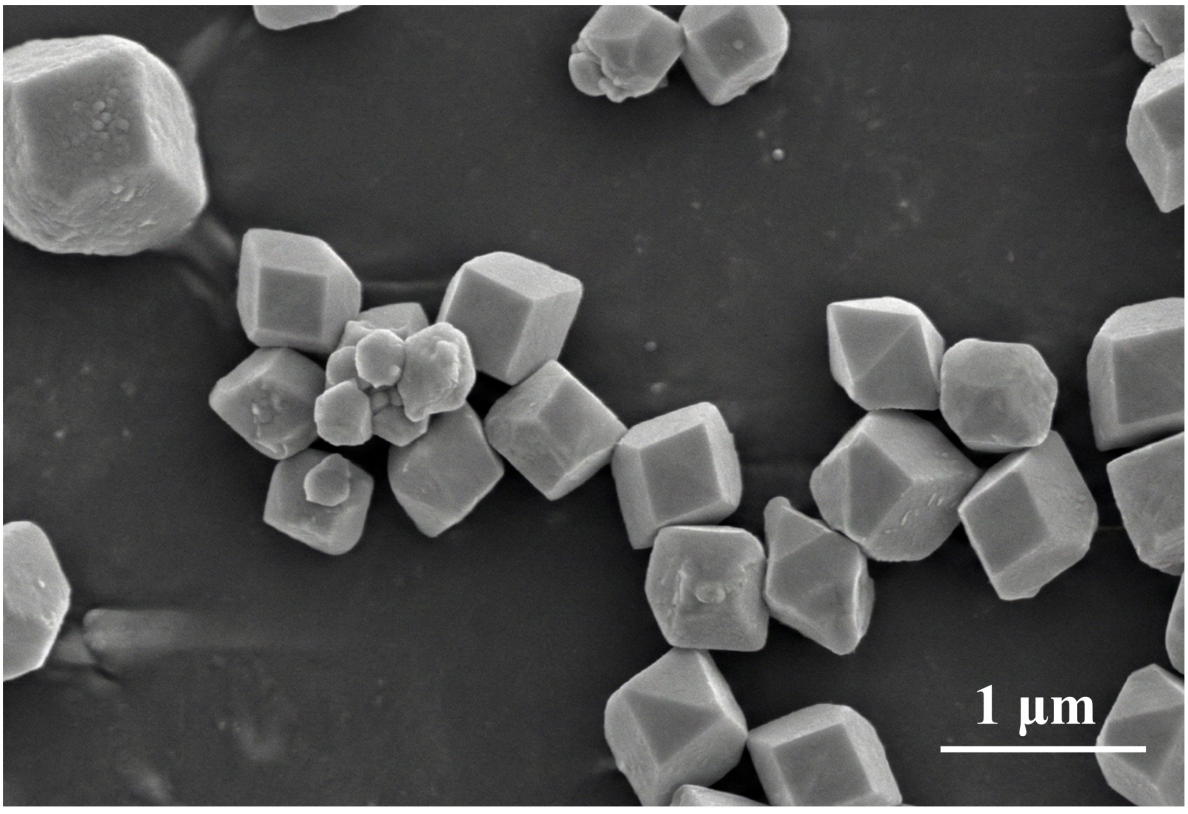

Figure 1: SEM image of the as-synthesized ZIF-67 precursor crystals, showing their uniform rhombic dodecahedral morphology.

The ZIF-67 precursor was subsequently subjected to pyrolysis at different temperatures (500, 600, 700, and 800 °C) under a N_2 atmosphere to induce its transformation into Co_3O_4/NC nanocomposites. The morphological evolution of the materials as a function of the pyrolysis temperature was investigated by SEM, as depicted in Figure 2. After pyrolysis at 500 °C (Co_3O_4/NC-500, Figure 2a), the dodecahedral morphology of the parent ZIF-67 is largely preserved, although the surfaces become rougher and a noticeable shrinkage in particle size to ~500 nm is observed due to the decomposition of the organic linkers. As the temperature increases to 600 °C (Co_3O_4/NC-600, Figure 2b) and 700 °C (Co_3O_4/NC-700, Figure 2c), the overall polyhedral shape is still maintained, but the structure becomes more porous and hollow, with a significant amount of carbonization occurring. The sample Co_3O_4/NC-700, in particular, displays a stable and highly porous framework, which is expected to provide abundant active sites and facilitate mass transport. However, when the temperature is further increased to 800 °C (Co_3O_4/NC-800, Figure 2d), the dodecahedral structure begins to collapse and aggregate, likely due to the excessive carbothermal reduction and sintering of cobalt species at such a high temperature [35]. This morphological analysis suggests that 700 °C is an optimal temperature for creating a well-defined, porous Co_3O_4/NC structure.

The elemental composition and distribution within the Co_3O_4/NC-700 nanocomposite were analyzed by EDS mapping, as shown in Figure 3. The maps clearly demonstrate the homogeneous distribution of carbon (C), nitrogen (N), oxygen (O), and cobalt (Co) elements throughout the entire dodecahedral structure. The strong correlation between the spatial distributions of Co and O confirms the formation of cobalt oxide, while the overlapping C and N signals verify the presence of an N-doped carbon framework. This uniform elemental distribution is crucial for ensuring that the catalytically active Co_3O_4 sites are readily accessible and well-integrated with the conductive carbon support.

3.2. Structural and compositional analysis

The crystallographic structure of the as-synthesized ZIF-67 and the pyrolyzed Co_3O_4/NC composites was investigated using XRD. As shown in Figure 4a, the XRD pattern of the ZIF-67 precursor exhibits a series of sharp diffraction peaks that are in excellent agreement with the simulated pattern, confirming its high crystallinity and pure phase [36]. After pyrolysis, the characteristic peaks of ZIF-67 disappear completely, indicating the

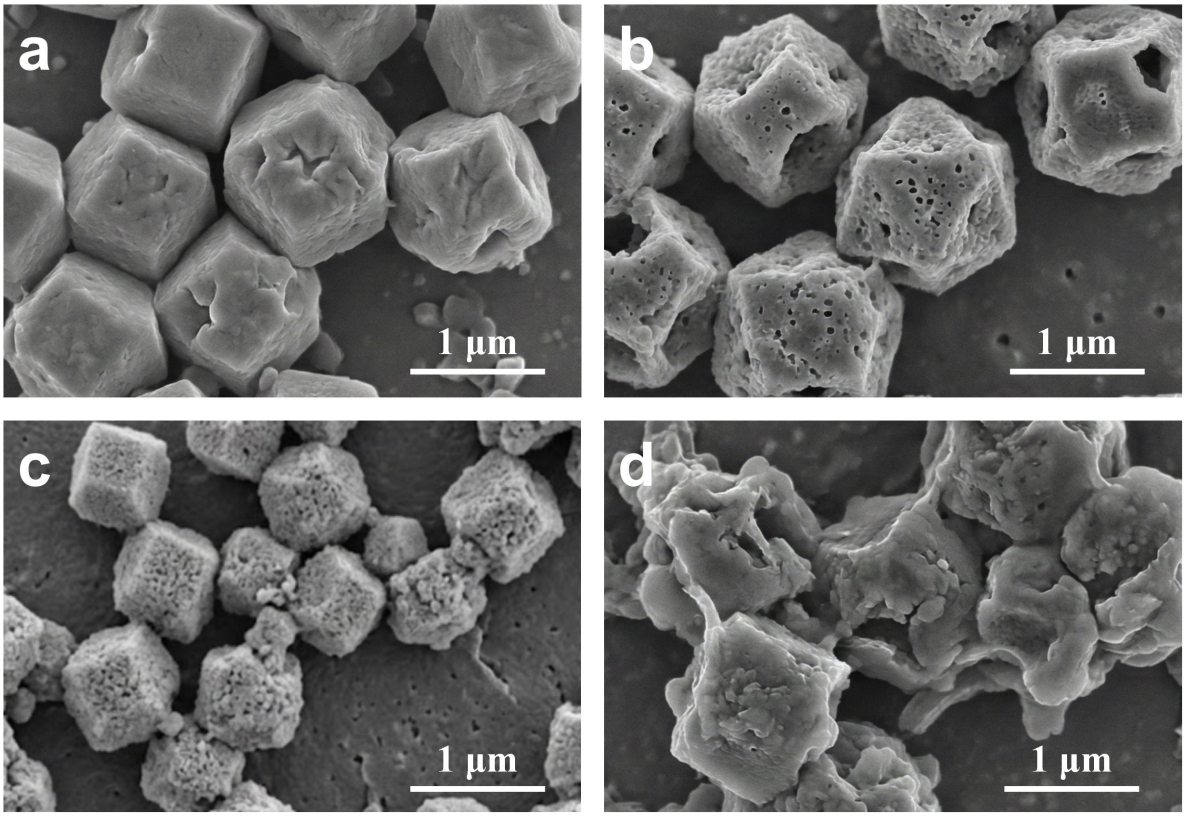

Figure 2: SEM images of the ZIF-67-derived nanocomposites prepared at different pyrolysis temperatures: (a) Co_3O_4/NC-500, (b) Co_3O_4/NC-600, (c) Co_3O_4/NC-700, and (d) Co_3O_4/NC-800. The images show the evolution from a solid dodecahedron to a porous and eventually collapsed structure.

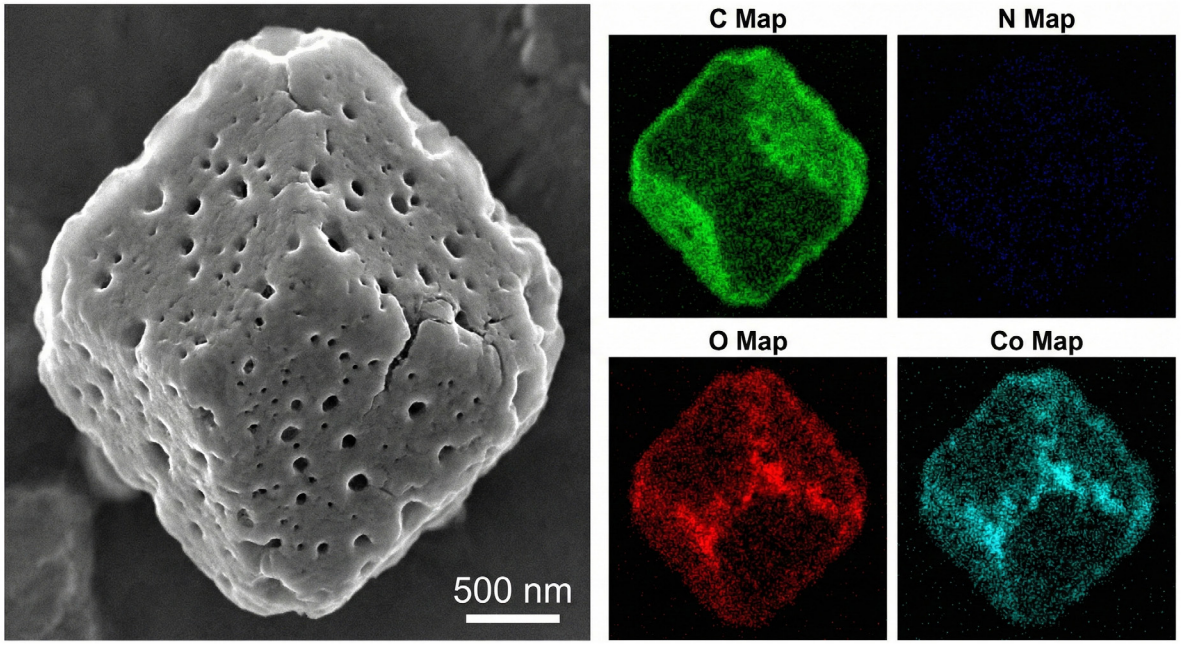

Figure 3: SEM image of a single Co_3O_4/NC-700 particle and the corresponding EDS elemental mapping for C, N, O, and Co.

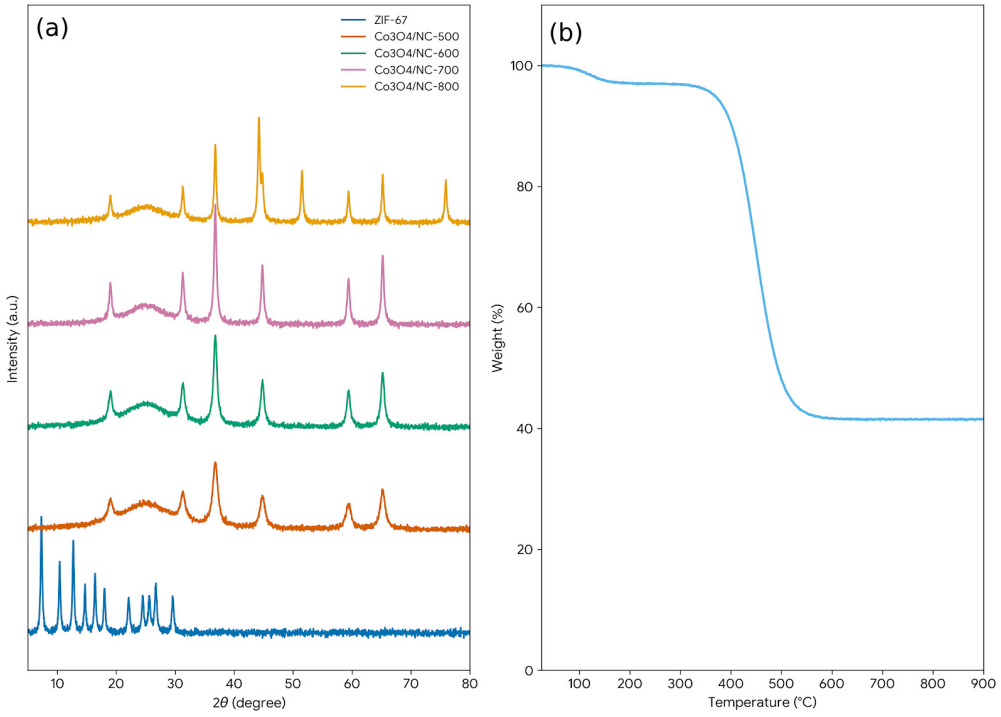

Figure 4: (a) XRD patterns of the ZIF-67 precursor and the Co_3O_4/NC composites pyrolyzed at different temperatures. (b) TGA curve of the ZIF-67 precursor measured under a N_2 atmosphere at a heating rate of 10 °C/min.

decomposition of the MOF structure. For the Co_3O_4/NC-500, -600, and -700 samples, the XRD patterns display distinct diffraction peaks at 2θ values of 19.0°, 31.3°, 36.8°, 44.8°, 59.4°, and 65.2°. These peaks can be indexed to the (111), (220), (311), (400), (511), and (440) crystal planes of the cubic spinel Co_3O_4 phase (JCPDS No. 42-1467) [34]. A broad peak centered around 25° is also observed, corresponding to the (002) plane of graphitic carbon, which confirms the formation of a carbonaceous matrix. Interestingly, for the Co_3O_4/NC-800 sample, additional sharp peaks appear at 44.2°, 51.5°, and 75.9°, which can be assigned to the (111), (200), and (220) planes of metallic cobalt (Co^0, JCPDS No. 15-0806). This indicates that at 800 °C, the Co_3O_4 is partially

reduced to metallic Co by the carbon matrix (carbothermal reduction), which can be detrimental to the desired electrocatalytic activity for nitrite oxidation. The average crystallite sizes of the Co_3O_4 phase, calculated using the Scherrer equation based on the (311) peak, are listed in Table 1. The size increases from 9.1 nm to 18.5 nm as the temperature rises from 500 °C to 800 °C, which is consistent with crystal growth at higher temperatures.

The thermal decomposition process of the ZIF-67 precursor was studied by TGA under a N_2 atmosphere, and the resulting curve is presented in Figure 4b. The initial slight weight loss of about 3% below 200 °C is attributed to the removal of adsorbed solvent molecules (methanol and water). The major weight loss of approximately 55% occurs in the temperature range of 350 °C to 550 °C, which corresponds to the thermal decomposition of the organic 2-methylimidazole linkers and the collapse of the ZIF-67 framework [36, 37]. The curve becomes stable after 600 °C, indicating that the organic components have been completely carbonized. The final residual weight is about 41.5%, which is close to the theoretical cobalt oxide content in ZIF-67. This TGA result guided the selection of the pyrolysis temperatures for the synthesis of the Co_3O_4/NC composites.

Raman spectroscopy was employed to investigate the nature of the carbon framework in the pyrolyzed composites. As shown in Figure 5a, all Co_3O_4/NC samples exhibit two prominent peaks at approximately 1352 cm^{-1} and 1595 cm^{-1}, corresponding to the D band (disordered and defect carbon) and the G band (graphitic sp^2 carbon), respectively. The intensity ratio of the D band to the G band (I(D)/I(G)) is often used to evaluate the degree of defects and graphitization in carbon materials. The calculated I(D)/I(G) ratios for Co_3O_4/NC-500, -600, -700, and -800 are 1.05, 0.98, 0.91, and 0.86, respectively. The decreasing trend of the I(D)/I(G) ratio with increasing pyrolysis temperature indicates a higher degree of graphitization in the carbon matrix, which is beneficial for enhancing its electrical conductivity. In addition to the carbon peaks, several weaker peaks are observed at 475, 518, and 680 cm^{-1}, which can be attributed to the Eg, F_2g, and A_1g vibrational modes of Co_3O_4, further confirming the presence of the cobalt oxide phase.

The porosity and specific surface area of the Co_3O_4/NC composites were characterized by N_2 adsorption-desorption analysis. The isotherms for all samples, shown in Figure 5b, display a type-IV curve with a distinct H3-type hysteresis loop at high relative pressures ($P/P_0 > 0.5$), which is characteristic of mesoporous materials [38]. The corresponding pore size distribution curves, calculated using the BJH method (Figure 5c), confirm the presence of mesopores, mainly centered around 4 nm and 20–40 nm. These mesopores are formed due to the release of gas molecules during the decomposition of the organic linkers. The key textural parameters are summarized in Table 2. The parent ZIF-67 exhibited a high BET surface area of 1654 m^2/g. After pyrolysis, the surface area decreases significantly due to the collapse of the microporous structure. Interestingly, the BET surface area first increases from 215.3 m^2/g for Co_3O_4/NC-500 to a maximum of 327.8 m^2/g for Co_3O_4/NC-700,

Table 1: Crystallite size of Co_3O_4 in the pyrolyzed samples calculated from the XRD patterns using the Scherrer equation.

SAMPLE	2θ of (311) PEAK (°)	FWHM (°)	Crystallite Size (nm)
Co_3O_4/NC-500	36.78	0.914	9.1
Co_3O_4/NC-600	36.82	0.735	11.3
Co_3O_4/NC-700	36.85	0.582	14.3
Co_3O_4/NC-800	36.88	0.451	18.5

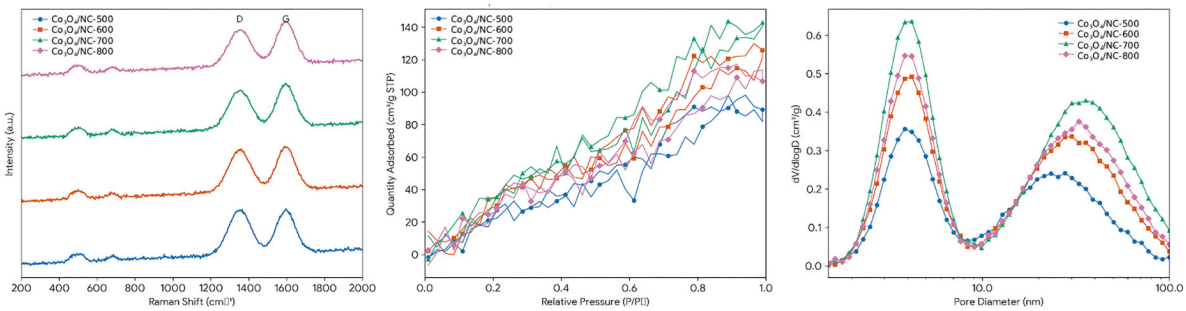

Figure 5: (a) Raman spectra of the Co_3O_4/NC composites prepared at different pyrolysis temperatures. (b) N_2 adsorption-desorption isotherms of the Co_3O_4/NC composites. (c) Pore size distribution curves of the Co_3O_4/NC composites derived from the BJH method.

and then decreases to 264.1 m^2/g for Co_3O_4/NC-800. The initial increase is due to the formation of more pores as the organic linkers are removed more completely. The subsequent decrease at 800 °C can be attributed to the partial collapse of the porous structure and pore blockage caused by the sintering of cobalt particles at high temperatures [25]. The Co_3O_4/NC-700 sample possesses the largest surface area and pore volume, which is highly advantageous for an electrochemical sensor as it can provide more active sites and facilitate the diffusion of electrolyte ions and analyte molecules.

3.3. Surface Chemical State Analysis (XPS)

X-ray photoelectron spectroscopy (XPS) was conducted to analyze the surface elemental composition and chemical states of the optimized Co_3O_4/NC-700 composite. The full survey spectrum (Figure 6a) confirms the presence of Co, O, N, and C elements on the surface of the material, which is consistent with the EDS results. The atomic percentages were calculated to be 68.2% for C, 15.5% for O, 11.1% for Co, and 5.2% for N.

The high-resolution Co 2p spectrum (Figure 6b) can be deconvoluted into two spin-orbit doublets (Co $2p_{3/2}$ and Co $2p_{1/2}$) and two corresponding satellite (Sat.) peaks. The peaks centered at binding energies of 780.1 eV and 795.0 eV are assigned to Co^{3+}, while the peaks at 782.0 eV and 797.2 eV correspond to Co^{2+} [39]. The presence of both Co^{2+} and Co^{3+} oxidation states is characteristic of the Co_3O_4 spinel structure, where Co^{2+} ions occupy tetrahedral sites and Co^{3+} ions occupy octahedral sites. The quantitative analysis of the peak areas reveals a Co^{3+}/Co^{2+} ratio of approximately 1.9, which is close to the theoretical value of 2 for Co_3O_4, further confirming the successful formation of the desired cobalt oxide phase.

The high-resolution C 1s spectrum (Figure 6c) is deconvoluted into three main components. The dominant peak at 284.8 eV corresponds to sp^2-hybridized carbon (C=C/C-C) from the graphitic carbon framework. The peak at 285.9 eV is attributed to C-N bonds, confirming the successful doping of nitrogen into the carbon lattice [40]. The third peak at 288.5 eV is assigned to C=O bonds, indicating some surface oxidation of the carbon material.

The high-resolution N 1s spectrum (Figure 6d) provides insight into the nature of nitrogen doping. The spectrum can be fitted into three distinct peaks, which are assigned to pyridinic-N (398.7 eV), pyrrolic-N (400.3 eV), and graphitic-N (401.5 eV) [41]. Pyridinic-N and pyrrolic-N are located at the edges or defects of the carbon layers and are known to be electrochemically active sites that can enhance catalytic performance. Graphitic-N, where a nitrogen atom substitutes a carbon atom within the graphitic plane, can improve the electrical conductivity of the carbon matrix. The presence of these multiple N species is highly beneficial for the electrochemical sensing application. The relative contents of different N species were analyzed for all samples and are presented in Table 3. With increasing pyrolysis temperature, the total nitrogen content decreases, and

Table 2: Textural properties of the ZIF-67 precursor and the pyrolyzed Co_3O_4/NC composites.

SAMPLE	BET SURFACE AREA (m^2/g)	TOTAL PORE VOLUME (cm^3/g)	AVERAGE PORE SIZE (nm)
ZIF-67	1654.2	0.785	1.9
Co_3O_4/NC-500	215.3	0.298	5.5
Co_3O_4/NC-600	289.6	0.412	5.7
Co_3O_4/NC-700	327.8	0.536	6.5
Co_3O_4/NC-800	264.1	0.451	6.8

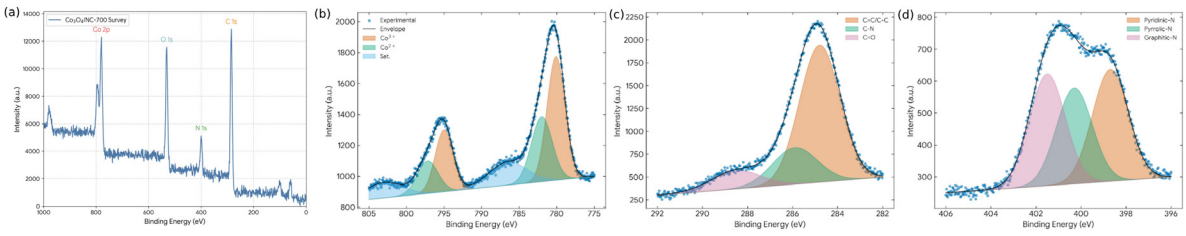

Figure 6: (a) XPS survey spectrum of Co_3O_4/NC-700. (b) High-resolution Co 2p spectrum. (c) High-resolution C 1s spectrum. (d) High-resolution N 1s spectrum.

the proportion of more stable graphitic-N increases at the expense of pyridinic-N and pyrrolic-N. The Co_3O_4/NC-700 sample appears to strike an optimal balance between the total N content and the distribution of different N species, contributing to its superior performance. The enhanced activity of Co_3O_4/NC-700 can be ascribed to the synergistic coupling of Co_3O_4 with the N-doped carbon matrix. Co_3O_4 provides redox-active Co sites, where the Co^{3+}/Co^{2+} couple facilitates nitrite oxidation, while the N-doped carbon improves charge transport and modulates the local electronic structure. Among the nitrogen species, pyridinic-N and pyrrolic-N are expected to contribute defect-associated active sites and stronger interfacial adsorption, whereas graphitic-N mainly enhances electronic conductivity. The superior performance of Co_3O_4/NC-700 is therefore attributed to the optimized balance between accessible Co_3O_4 active centers, sufficient N functionality, and improved graphitization.

3.4. Electrochemical performance for nitrite detection

To evaluate the potential of the synthesized materials for electrochemical sensing, we first investigated the electrochemical properties of the modified electrodes using CV and EIS. Figure 7a shows the CV curves of a bare GCE and GCEs modified with the different Co_3O_4/NC composites in 0.1 M PBS. The modified electrodes all exhibit a significantly larger capacitive background current compared to the bare GCE, which is attributed to their large surface area. Among them, the Co_3O_4/NC-700/GCE shows the largest background current, consistent with its highest BET surface area. The electron transfer kinetics at the electrode-electrolyte interface were studied by EIS, and the Nyquist plots are shown in Figure 7b. The diameter of the semicircle in the high-frequency region represents the charge transfer resistance (Rct). The bare GCE shows a large semicircle with an Rct of ~1250 Ω. After modification, the Rct values decrease dramatically, indicating that the composites facilitate electron transfer. The Rct values for Co_3O_4/NC-500, -600, -700, and -800 modified electrodes are calculated to be 210, 135, 65, and 98 Ω, respectively. The Co_3O_4/NC-700/GCE exhibits the smallest Rct, suggesting the fastest electron transfer kinetics. This can be attributed to its optimal combination of high surface area, porous structure, and good electrical conductivity from the more graphitized carbon matrix.

The applied potential was optimized because nitrite oxidation is strongly potential-dependent. Although the oxidation current further increased slightly above +0.80 V, the background current and noise also increased; therefore, +0.80 V provided the best compromise between sensitivity and analytical stability.

The electrocatalytic activity of the prepared sensors towards nitrite oxidation was then investigated. Figure 8a displays the CVs of the Co_3O_4/NC-700/GCE in the absence and presence of 1.0 mM $NaNO_2$ in

Table 3: Surface elemental composition and relative content of different N species in the Co_3O_4/NC composites determined by XPS.

SAMPLE	N (at. %)	PYRIDINIC-N (%)	PYRROLIC-N (%)	GRAPHITIC-N (%)
Co_3O_4/NC-500	8.9	45.1	38.6	16.3
Co_3O_4/NC-600	6.7	40.2	35.5	24.3
Co_3O_4/NC-700	5.2	34.8	30.1	35.1
Co_3O_4/NC-800	3.1	25.6	21.7	52.7

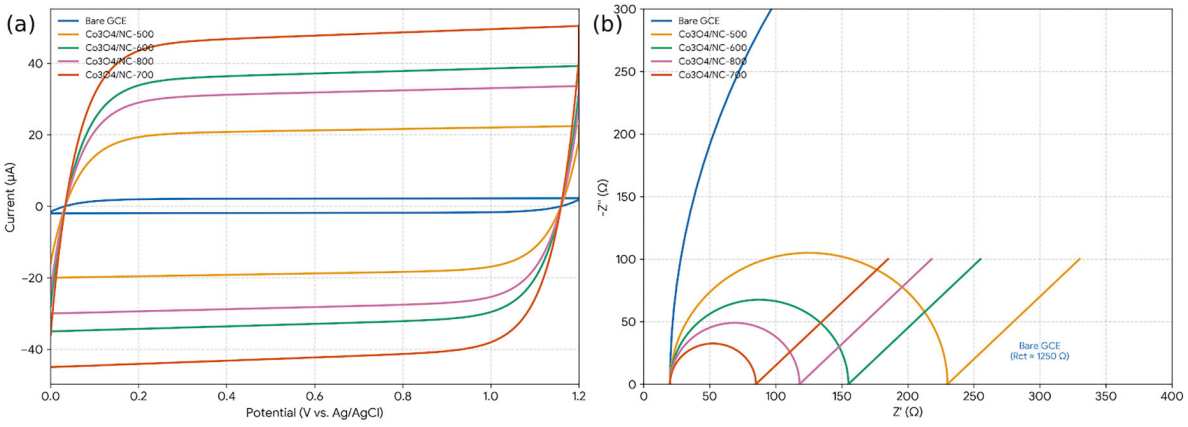

Figure 7: (a) CVs of bare GCE and GCEs modified with different Co_3O_4/NC composites in 0.1 M PBS (pH 7.0) at a scan rate of 50 mV/s. (b) EIS Nyquist plots of the different electrodes in 5.0 mM $[Fe(CN)_6]^{3-/4-}$ + 0.1 M KCl.

0.1 M PBS. No significant redox peaks are observed in the absence of nitrite. However, upon the addition of nitrite, a distinct and well-defined irreversible oxidation peak appears at a potential of approximately +0.82 V (vs. Ag/AgCl), indicating that the Co_3O_4/NC-700 composite has excellent electrocatalytic activity for nitrite oxidation. The electrochemical oxidation of nitrite on the electrode surface likely proceeds via the reaction: $NO_2^- + H_2O \rightarrow NO_3^- + 2H^+ + 2e^-$. The Co^{3+}/Co^{2+} redox couple on the surface of Co_3O_4 nanoparticles is believed to act as the catalytic active center that mediates this electron transfer process. The oxidation peak potential of nitrite on Co_3O_4/NC-700/GCE is centered at ca. +0.82 V (vs. Ag/AgCl), so +0.80 V was selected for amperometric detection to maximize faradaic response while remaining slightly below the peak maximum. Additional comparison experiments at +0.70, +0.75, +0.80, and +0.85 V showed that +0.80 V provided the highest signal-to-noise ratio and the most stable baseline. At +0.70 V, the nitrite response was detectable but markedly lower; therefore, +0.80 V was retained as the optimum operating potential for this material. The superior response of Co_3O_4/NC-700 compared with bare-oxide-type systems can be attributed not only to the catalytic Co_3O_4 phase, but also to the ZIF-67-derived porous N-doped carbon scaffold, which lowers Rct, improves dispersion of active sites, and facilitates nitrite diffusion.

The performance of the sensors prepared with materials pyrolyzed at different temperatures was compared, as shown in Figure 8b. Under the same conditions, the oxidation peak current for nitrite follows the order: Co_3O_4/NC-700 > Co_3O_4/NC-600 > Co_3O_4/NC-800 > Co_3O_4/NC-500. The Co_3O_4/NC-700/GCE exhibits the highest catalytic current, which is consistent with its superior structural properties, including the largest surface area, optimal porosity, and lowest charge transfer resistance. The lower activity of the Co_3O_4/NC-500 and -600 samples can be attributed to their lower conductivity and smaller surface area. The decreased activity of the Co_3O_4/NC-800 sample is likely due to its collapsed structure, reduced surface area, and the presence of less active metallic Co.

The effect of scan rate on the electrochemical response of the Co_3O_4/NC-700/GCE was also studied (Figure 8c). The oxidation peak current increases linearly with the square root of the scan rate ($v^{1/2}$) from

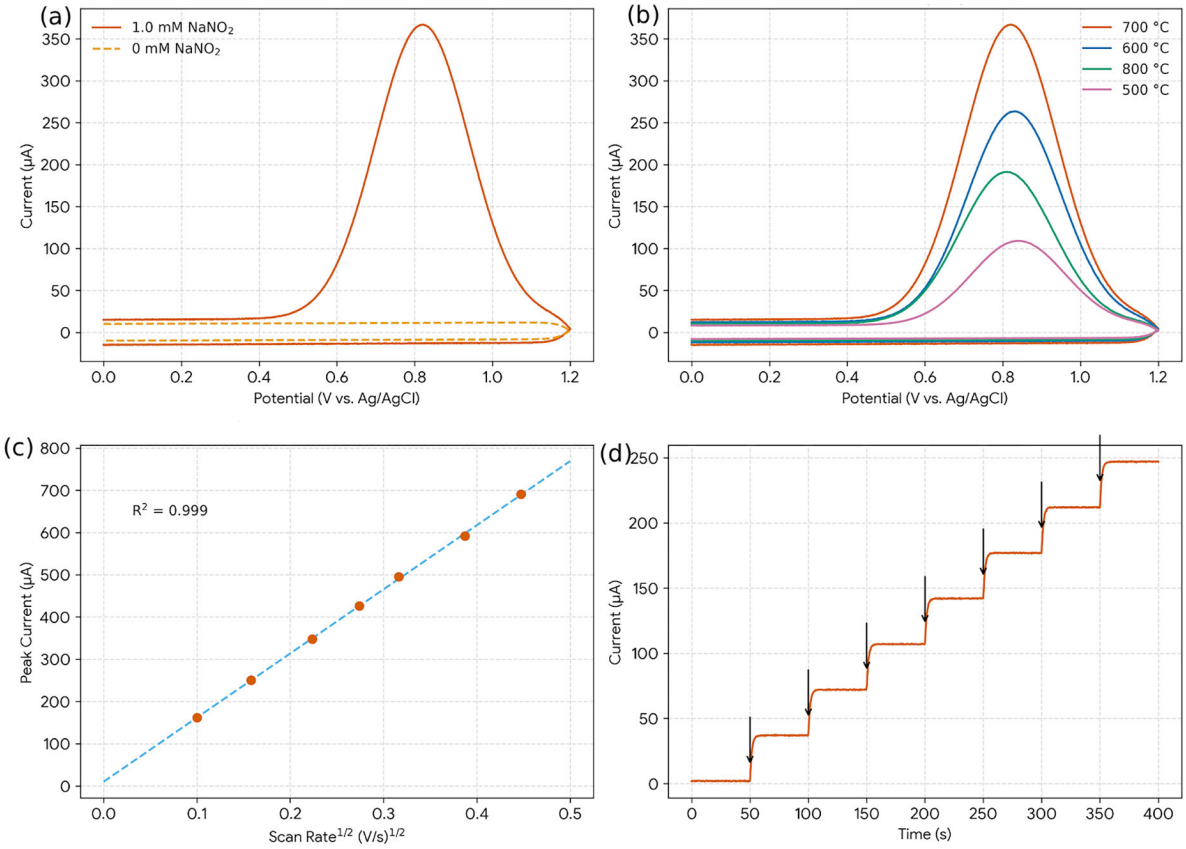

Figure 8: (a) CVs of Co_3O_4/NC-700/GCE in 0.1 M PBS (pH 7.0) without and with 1.0 mM $NaNO_2$. (b) CVs of different Co_3O_4/NC-T/GCEs in 1.0 mM $NaNO_2$. (c) The relationship between the peak current and the square root of the scan rate for Co_3O_4/NC-700/GCE. (d) Amperometric response of Co_3O_4/NC-700/GCE to successive additions of $NaNO_2$ at an applied potential of +0.80 V.

10 to 200 mV/s, with a linear regression equation of Ipa (μA) = 45.2 $v^{1/2}$ $(V/s)^{1/2}$ + 8.1 (R^2 = 0.998). This linear relationship indicates that the electro-oxidation of nitrite on the Co_3O_4/NC-700/GCE is a diffusion-controlled process.

Amperometry (i-t curve) was used for the quantitative determination of nitrite due to its higher sensitivity. Figure 8d shows the typical amperometric response of the Co_3O_4/NC-700/GCE upon successive additions of nitrite into a stirred PBS solution at an applied potential of +0.80 V. The current increases rapidly in a stepwise manner with each addition of nitrite, reaching a steady state within 3 seconds. This demonstrates the sensor's rapid and sensitive response to changes in nitrite concentration.

The calibration curve for the Co_3O_4/NC-700 sensor is plotted in Figure 9a. The response current is linearly proportional to the nitrite concentration over a wide range. As shown in Figure 9b, there are two distinct linear ranges: a lower range from 0.1 μM to 100 μM with a regression equation of I (μA) = 0.601 C (μM) + 0.15 (R^2 = 0.999), and a higher range from 100 μM to 1500 μM with an equation of I (μA) = 0.355 C (μM) + 25.1 (R^2 = 0.997). The sensitivity, calculated from the slope of the calibration curve and the electrode area (0.0707 cm^2), is 850.3 μA mM^{-1} cm^{-2} for the lower concentration range. The limit of detection (LOD) was calculated from the calibration plot using the 3σ/S criterion, where σ is the standard deviation of the blank current obtained from repeated measurements of blank PBS under identical amperometric conditions and S is the slope of the low-concentration calibration plot. Thus, the reported LOD of 0.03 μM was obtained from the analytical calibration method rather than from the standard addition procedure. The standard addition method was used only for the quantification of nitrite in real water samples and recovery evaluation. The analytical performance parameters for all prepared sensors are summarized in Table 4, which clearly confirms the superiority of the Co_3O_4/NC-700 sensor. The two linear ranges likely originate from a concentration-dependent change in the dominant kinetic regime. At low nitrite concentrations, abundant exposed catalytic sites and rapid interfacial electron transfer lead to a steeper slope. At higher concentrations, partial occupation of active sites and increased diffusion/transport limitation reduce the apparent sensitivity, giving rise to a second linear region. For quantification near the boundary concentration (around 100 μM), calibration should therefore be performed using the appropriate local linear segment.

The selectivity of the Co_3O_4/NC-700 sensor is a crucial parameter for its practical application. The amperometric response to 100 μM nitrite was measured in the presence of various potentially interfering

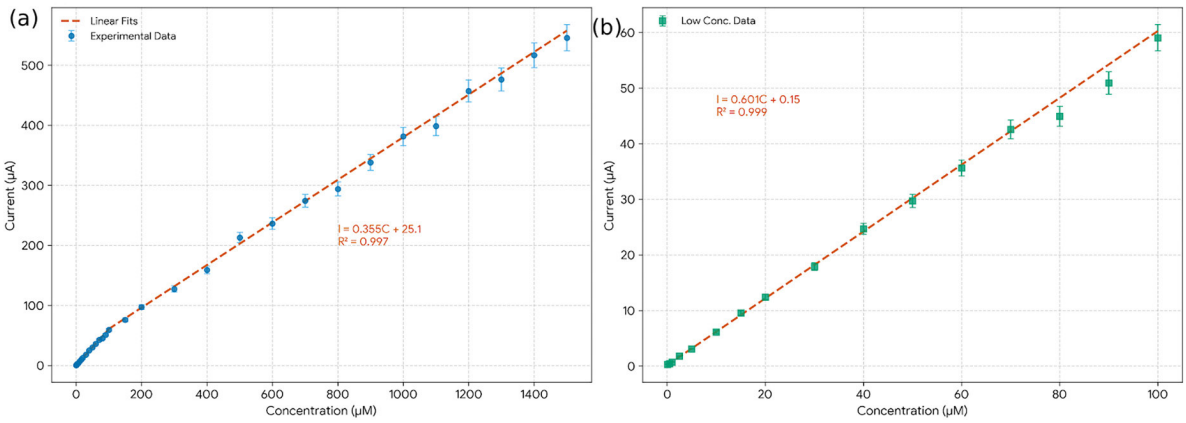

Figure 9: (a) Calibration curve of the current response versus nitrite concentration for the Co_3O_4/NC-700/GCE. (b) The corresponding two linear ranges, values are presented as mean ± SD (n = 3).

Table 4: Comparison of the analytical performance of the different Co_3O_4/NC-T/GCEs for nitrite detection.

SENSOR	LINEAR RANGE (μM)	SENSITIVITY (μA mM^{-1} cm^{-2})	LOD (μM) (S/N=3)	R^2
Co_3O_4/NC-500/GCE	1.0 – 800	255.1	0.85	0.992
Co_3O_4/NC-600/GCE	0.5 – 1200	489.3	0.21	0.996
Co_3O_4/NC-700/GCE	0.1 – 1500	850.3	0.03	0.999
Co_3O_4/NC-800/GCE	0.8 – 1000	376.9	0.47	0.994

species. In addition to K^+, Na^+, Cl^-, SO_4^{2-}, NO_3^-, glucose, ascorbic acid, and uric acid, we further evaluated representative interferents relevant to natural waters, including humic acid, sulfite, Ca^{2+}, Mg^{2+}, Cu^{2+}, Fe^{3+}, and sodium dodecyl sulfate. Under the tested concentrations, these species caused only minor changes in the nitrite response, confirming the robustness of the sensor matrix. Residual free chlorine and other strong oxidants may interfere at positive detection potentials; therefore, freshly collected or dechlorinated samples are recommended for practical analysis. This indicates the excellent anti-interference ability and high selectivity of the sensor.

The reproducibility and stability of the sensor were also evaluated. The relative standard deviation (RSD) for seven successive measurements of 100 μM nitrite with the same electrode was 2.8%. The electrode-to-electrode reproducibility was assessed by fabricating five independent sensors, which yielded an RSD of 3.9% (Figure 10a), demonstrating good fabrication reproducibility. For the long-term stability test (Figure 10b), the sensor was stored at 4 °C when not in use and tested periodically. After 30 days of storage at 4 °C, the sensor retained 94.5% of its initial current response, indicating good short-term storage stability. Extended storage stability (2–3 months), continuous-use drift, and cycling durability were not fully investigated in the present work and will be addressed in future studies.

The performance of our Co_3O_4/NC-700 sensor was compared with other previously reported electrochemical sensors for nitrite, as summarized in Table 5. It is evident that our sensor exhibits a comparable or superior performance, particularly in terms of its wide linear range, high sensitivity, and very low detection limit. This outstanding performance highlights the significant advantages of the unique porous structure derived from the ZIF-67 template.

To validate its practical applicability, the Co_3O_4/NC-700 sensor was used to determine the nitrite concentration in real water samples (tap water and local river water) using the standard addition method. The results (Table 6) demonstrated recovery rates between 98.6% and 103.2%, which are in good agreement with the results obtained from a standard spectrophotometric method. This confirms that the developed sensor is reliable and suitable for the practical determination of nitrite in real environmental samples.

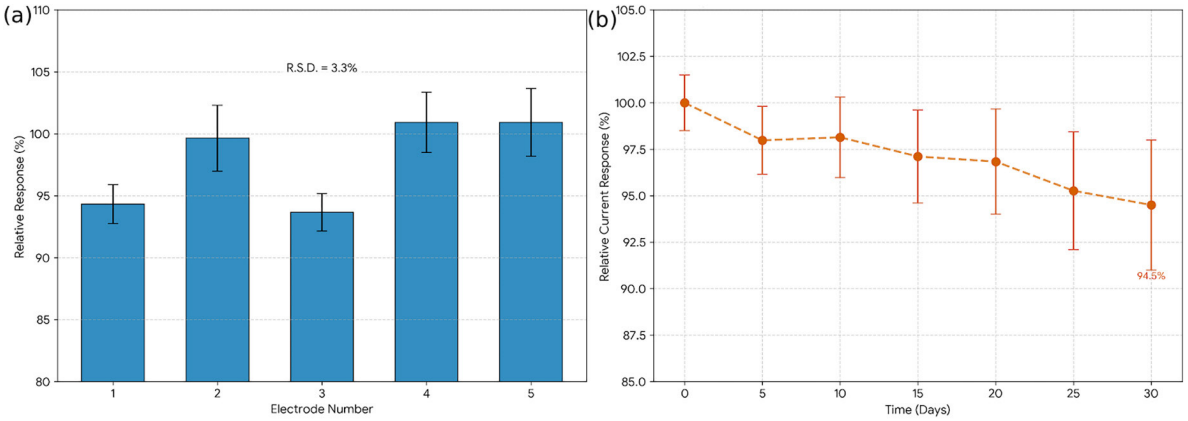

Figure 10: (a) Reproducibility test using five independently prepared electrodes (n = 5). (b) Long-term stability of the sensor stored at 4 °C over 30 days (n = 3).

Table 5: Comparison of the analytical performance of the Co_3O_4/NC-700/GCE with other reported nitrite sensors.

ELECTRODE MATERIAL	LINEAR RANGE (μM)	LOD (μM)	SENSITIVITY (μA mM^{-1} cm^{-2})	REFERENCE
Co_3O_4 circular sheets	6.6 – 3000	0.22	318	[8]
Spindle-like Co_3O_4/rGO	1 – 380	0.14	–	[42]
Co_3O_4-rGO/CNTs	8 – 56000	0.016	–	[43]
AuNPs/Co_3O_4/Graphene	0.2 – 2500	0.05	–	[44]
ZIF-67C/CuO-NiO	2 – 1718	0.58	732	[45]
Co_3O_4/NC-700 (This work)	**0.1 – 1500**	**0.03**	**850.3**	–

Table 6: Determination of nitrite in real water samples using the Co_3O_4/NC-700/GCE sensor by the standard addition method.

SAMPLE	ADDED (μM)	FOUND (μM)	RECOVERY (%)	RSD (%)
Tap water	20.0	19.7	98.6	2.4
Tap water	100.0	101.8	101.8	2.1
River water	50.0	51.6	103.2	2.8
River water	200.0	198.9	99.5	2.3

4. CONCLUSION

In this work, the principal novelty is not merely the preparation of a Co_3O_4-based nitrite sensor, but the demonstration that the pyrolysis temperature of a single ZIF-67 precursor governs the balance among porosity, graphitization, cobalt speciation, and nitrogen functionality, which together determine nitrite-sensing performance. Among the materials examined, Co_3O_4/NC-700 provided the most favorable structural combination: a preserved porous dodecahedral framework, the highest BET surface area, the lowest charge-transfer resistance, and a balanced distribution of catalytically useful N species. These features translated into fast and sensitive nitrite oxidation, with reliable operation in real water samples. The results indicate that ZIF-67-derived Co_3O_4/N-doped carbon is an effective electrode design strategy because it integrates catalytic oxide sites with a conductive defect-rich carbon network in a single step. More broadly, this study provides a practical structure–property guideline for tailoring MOF-derived composite electrodes for environmental electroanalysis.

5. BIBLIOGRAPHY

[1] SHRIVASTAV, V., MANSI, DUBEY, P., *et al.*, "Analyzing the charge contributions of metal–organic framework derived nanosized cobalt nitride/carbon composites in asymmetrical supercapacitors", *Nanoscale Advances*, v. 6, n. 16, pp. 4219–4229, Aug. 2024. doi: https://doi.org/10.1039/D4NA00291A. PubMed PMID: 39114156.

[2] PICETTI, R., DEENEY, M., PASTORINO, S., *et al.*, "Nitrate and nitrite contamination in drinking water and cancer risk: A systematic review with meta-analysis", *Environmental Research*, v. 210, pp. 112988, Jul. 2022. doi: https://doi.org/10.1016/j.envres.2022.112988. PubMed PMID: 35217009.

[3] MUN, S.H., PARK, G.J., LEE, J.H., *et al.*, "Two cases of fatal methemoglobinemia caused by self-poisoning with sodium nitrite: A case report", *Medicine*, v. 101, n. 7, pp. e28810, Feb. 2022. doi: https://doi.org/10.1097/MD.0000000000028810. PubMed PMID: 35363170.

[4] YANG, H., CHENG, H., "Controlling nitrite level in drinking water by chlorination and chloramination", *Separation and Purification Technology*, v. 56, n. 3, pp. 392–396, Sep. 2007. doi: https://doi.org/10.1016/j.seppur.2007.05.036.

[5] GAJDÁR, J., RODRIGUES GASPAR, S., ALMEIDA, M.G., "Trends in nitrite detection: Recent advances in electrochemical sensor technologies", *Trends in Analytical Chemistry*, v. 183, pp. 118105, Feb. 2025. doi: https://doi.org/10.1016/j.trac.2024.118105.

[6] ASLAM, M., ALI, S., HAMDY, K., *et al.*, "Progress in electrode modifiers for nitrite electrochemical sensing applications", *Biosensors*, v. 15, n. 12, pp. 783, Nov. 2025. doi: https://doi.org/10.3390/bios15120783. PubMed PMID: 41440264.

[7] ZHE, T., LI, M., LI, F., *et al.*, "Integrating electrochemical sensor based on MoO_3/Co_3O_4 heterostructure for highly sensitive sensing of nitrite in sausages and water", *Food Chemistry*, v. 367, pp. 130666, Jan. 2022. doi: https://doi.org/10.1016/j.foodchem.2021.130666. PubMed PMID: 34343805.

[8] SUDHA, V., MOHANTY, S.A., THANGAMUTHU, R., "Facile synthesis of Co_3O_4 disordered circular sheets for selective electrochemical determination of nitrite", *New Journal of Chemistry = Nouveau Journal de Chimie*, v. 42, n. 14, pp. 11869–11877, Jul. 2018. doi: https://doi.org/10.1039/C8NJ02639D.

[9] AHMED, M.S., CHOI, B., KIM, Y.-B., "Development of highly active bifunctional electrocatalyst using Co_3O_4 on carbon nanotubes for oxygen reduction and oxygen evolution", *Scientific Reports*, v. 8, n. 1, pp. 2543, Feb. 2018. doi: https://doi.org/10.1038/s41598-018-20974-1. PubMed PMID: 29416089.

[10] FAN, L., WANG, Z., WANG, Y., *et al.*, "Exploiting synergistic effects: Co_3O_4/g-C_3N_4 composite catalyst for enhanced oxygen evolution reaction", *International Journal of Electrochemical Science*, v. 18, n. 12, pp. 100394, Dec. 2023. doi: https://doi.org/10.1016/j.ijoes.2023.100394.

[11] LIU, X., LIU, H., MI, M., *et al.*, "Nitrogen-doped hierarchical porous carbon aerogel for high-performance capacitive deionization", *Separation and Purification Technology*, v. 224, pp. 44–50, Oct. 2019. doi: https://doi.org/10.1016/j.seppur.2019.05.010.

[12] WU, B., MENG, H., MORALES, D.M., *et al.*, "Nitrogen-rich carbonaceous materials for advanced oxygen electrocatalysis: synthesis, characterization, and activity of nitrogen sites", *Advanced Functional Materials*, v. 32, n. 31, pp. 2204137, 2022. doi: https://doi.org/10.1002/adfm.202204137.

[13] ULLAH, M., GANESAN, S., KUMARI, B., *et al.*, "A novel ZIF-67@g-C_3N_4–based colorimetric sensor with large hierarchical structure and enhanced surface area for sensitive detection of nitrite in drinking water", *Ionics*, v. 30, n. 10, pp. 6705–6718, Oct. 2024. doi: https://doi.org/10.1007/s11581-024-05756-2.

[14] ULLAH, M., KANJARIYA, P., REKHA, M.M., *et al.*, "Fabrication of an electrochemical sensor based on g-C_3N_4–NiO nanocomposite for sensitive and selective detection of hydrogen peroxide", *Journal of Materials Science Materials in Electronics*, v. 36, n. 17, pp. 1061, Jun. 2025. doi: https://doi.org/10.1007/s10854-025-15091-5.

[15] ULLAH, M., ZHENGXIN, L., TIRTH, V., "Highly sensitive and selective colorimetric sensing of nitrite based on largest surface area ZIF-67 nanostructure with enhanced peroxidase catalytic activities", *Journal of Materials Science Materials in Electronics*, v. 35, n. 24, pp. 1633, Aug. 2024. doi: https://doi.org/10.1007/s10854-024-13387-6.

[16] ULLAH, M., ARSHAD, M., WEI, C.R., *et al.*, "Rational designing of ZIF-67-derived Co_3O_4 nanocomposite with hierarchical porous structure and extensive peroxidase mimetic activities for highly sensitive colorimetric detection of nitrite in drinking water", *Mikrochimica Acta*, v. 192, n. 2, pp. 61, Feb. 2025. doi: https://doi.org/10.1007/s00604-024-06904-1. PubMed PMID: 39779597.

[17] SHEN, K., CHEN, X., CHEN, J., *et al.*, "Development of MOF-derived carbon-based nanomaterials for efficient catalysis", *ACS Catalysis*, v. 6, n. 9, pp. 5887–5903, Sep. 2016. doi: https://doi.org/10.1021/acscatal.6b01222.

[18] LU, X.F., FANG, Y., LUAN, D., *et al.*, "Metal–organic frameworks derived functional materials for electrochemical energy storage and conversion: A mini review", *Nano Letters*, v. 21, n. 4, pp. 1555–1565, Feb. 2021. doi: https://doi.org/10.1021/acs.nanolett.0c04898. PubMed PMID: 33567819.

[19] PHAN, A., DOONAN, C.J., URIBE-ROMO, F.J., *et al.*, "Synthesis, structure, and carbon dioxide capture properties of zeolitic imidazolate frameworks", *Accounts of Chemical Research*, v. 43, n. 1, pp. 58–67, Jan. 2010. doi: https://doi.org/10.1021/ar900116g. PubMed PMID: 19877580.

[20] PAN, Y., LI, H., ZHANG, X.-X., *et al.*, "Large-scale synthesis of ZIF-67 and highly efficient carbon capture using a ZIF-67/glycol-2-methylimidazole slurry", *Chemical Engineering Science*, v. 137, pp. 504–514, Dec. 2015. doi: https://doi.org/10.1016/j.ces.2015.06.069.

[21] LI, W., ZHANG, A., JIANG, X., *et al.*, "Low temperature CO_2 methanation: ZIF-67-derived co-based porous carbon catalysts with controlled crystal morphology and size", *ACS Sustainable Chemistry & Engineering*, v. 5, n. 9, pp. 7824–7831, Sep. 2017. doi: https://doi.org/10.1021/acssuschemeng.7b01306.

[22] WU, Y., WANG, Y., XIAO, Z., *et al.*, "Electrocatalytic oxygen reduction by a Co/Co_3O_4@N-doped carbon composite material derived from the pyrolysis of ZIF-67/poplar flowers", *RSC Advances*, v. 11, n. 5, pp. 2693–2700, Jan. 2021. doi: https://doi.org/10.1039/D0RA09615F. PubMed PMID: 35424214.

[23] SHAHZADI, S., AKHTAR, M., ARSHAD, M., *et al.*, "A review on synthesis of MOF-derived carbon composites: innovations in electrochemical, environmental and electrocatalytic technologies", *RSC Advances*, v. 14, n. 38, pp. 27575–27607, 2024. doi: https://doi.org/10.1039/D4RA05183A. PubMed PMID: 39228752.

[24] CHEN, T.-Y., LIN, L.-Y., GENG, D.-S., *et al.*, "Systematic synthesis of ZIF-67 derived Co_3O_4 and N-doped carbon composite for supercapacitors via successive oxidation and carbonization", *Electrochimica Acta*, v. 376, pp. 137986, Apr. 2021. doi: https://doi.org/10.1016/j.electacta.2021.137986.

[25] LI, Y.-M., LIU, Z.-Y., ZHANG, Q.-Y., *et al.*, "Influence of carbonization temperature on cobalt-based nitrogen-doped carbon nanopolyhedra derived from ZIF-67 for nonoxidative propane dehydrogenation", *Petroleum Science*, v. 20, n. 1, pp. 559–568, Feb. 2023. doi: https://doi.org/10.1016/j.petsci.2022.01.008.

[26] SARIOĞLAN, A., AGHAMOHAMMADI, S., AGHDAEI, Y.F., *et al.*, "ZIF-67 based nano sized-cobalt oxides via pyrolysis and cold plasma treatments for Fischer–Tropsch synthesis", *Molecular Catalysis*, v. 583, pp. 115217, Aug. 2025. doi: https://doi.org/10.1016/j.mcat.2025.115217.

[27] TAN, S., FAN, M., TU, W., *et al.*, "Crystalline-amorphous Co/Co_3O_4 derived from a low-temperature etching of ZIF-67 for oxygen-invovled catalytic reactions", *Applied Surface Science*, v. 640, pp. 158266, Dec. 2023. doi: https://doi.org/10.1016/j.apsusc.2023.158266.

[28] YANG, X., CHEN, J., CHEN, Y., *et al.*, "Novel Co_3O_4 nanoparticles/nitrogen-doped carbon composites with extraordinary catalytic activity for Oxygen Evolution Reaction (OER)", *Nano-Micro Letters*, v. 10, n. 1, pp. 15, Nov. 2017. doi: https://doi.org/10.1007/s40820-017-0170-4. PubMed PMID: 30393664.

[29] SADIQ, S., KHAN, I., HUMAYUN, M., *et al.*, "Synthesis of metal–organic framework-based ZIF-8@ ZIF-67 nanocomposites for antibiotic decomposition and antibacterial activities", *ACS Omega*, v. 8, n. 51, pp. 49244–49258, Dec. 2023. doi: https://doi.org/10.1021/acsomega.3c07606. PubMed PMID: 38162750.

[30] DIOP, N.F., OTUN, K.O., THIOR, S., *et al.*, "Facile room-temperature solution-phase synthesis of a ZIF-67 : Ni hybrid-MOF battery type material for supercapacitor applications", *RSC Advances*, v. 15, n. 42, pp. 34976–34990, Sep. 2025. doi: https://doi.org/10.1039/D5RA05741H. PubMed PMID: 40995348.

[31] MOHTASHAM, H., ROSTAMI, M., GHOLIPOUR, B., *et al.*, "Nano-architecture of MOF (ZIF-67)-based Co3O4 NPs@N-doped porous carbon polyhedral nanocomposites for oxidative degradation of antibiotic sulfamethoxazole from wastewater", *Chemosphere*, v. 310, pp. 136625, Jan. 2023. doi: https://doi.org/10.1016/j.chemosphere.2022.136625. PubMed PMID: 36181853.

[32] BARRETT, E.P., JOYNER, L.G., HALENDA, P.P., "The determination of pore volume and area distributions in porous substances. I. Computations from nitrogen isotherms", *Journal of the American Chemical Society*, v. 73, n. 1, pp. 373–380, Jan. 1951. doi: https://doi.org/10.1021/ja01145a126.

[33] FENG, X., WU, T., CARREON, M.A., "Synthesis of ZIF-67 and ZIF-8 crystals using DMSO (Dimethyl Sulfoxide) as solvent and kinetic transformation studies", *Journal of Crystal Growth*, v. 455, pp. 152–156, Dec. 2016. doi: https://doi.org/10.1016/j.jcrysgro.2016.10.016.

[34] REN, Q., FENG, Z., MO, S., *et al.*, "1D-Co_3O_4, 2D-Co_3O_4, 3D-Co_3O_4 for catalytic oxidation of toluene", *Catalysis Today*, v. 332, pp. 160–167, Jul. 2019. doi: https://doi.org/10.1016/j.cattod.2018.06.053.

[35] SONG, X., YU, J., WEI, M., *et al.*, "Ionic liquids-functionalized zeolitic imidazolate framework for carbon dioxide adsorption", *Materials*, v. 12, n. 15, pp. 2361, Jul. 2019. doi: https://doi.org/10.3390/ma12152361. PubMed PMID: 31349539.

[36] DAVOODI, M., DAVAR, F., REZAYAT, M.R., *et al.*, "Cobalt metal–organic framework-based ZIF-67 for the trace determination of herbicide molinate by ion mobility spectrometry: investigation of different morphologies", *RSC Advances*, v. 11, n. 5, pp. 2643–2655, Jan. 2021. doi: https://doi.org/10.1039/D0RA09298C. PubMed PMID: 35424212.

[37] FRANK, S., FOLKJÆR, M., NIELSEN, M.L.N., *et al.*, "Correlating the structural transformation and properties of ZIF-67 during pyrolysis, towards electrocatalytic oxygen evolution", *Journal of Materials Chemistry. A, Materials for Energy and Sustainability*, v. 12, n. 2, pp. 781–794, 2024. doi: https://doi.org/10.1039/D3TA05293A.

[38] THOMMES, M., KANEKO, K., NEIMARK, A.V., *et al.*, "Physisorption of gases, with special reference to the evaluation of surface area and pore size distribution (IUPAC Technical Report)", *Pure and Applied Chemistry*, v. 87, n. 9–10, pp. 1051–1069, Oct. 2015. doi: https://doi.org/10.1515/pac-2014-1117.

[39] CHEN, H., YANG, M., LIU, Y., *et al.*, "Influence of Co_3O_4 nanostructure morphology on the catalytic degradation of p-Nitrophenol", *Molecules*, v. 28, n. 21, pp. 7396, Nov. 2023. doi: https://doi.org/10.3390/molecules28217396. PubMed PMID: 37959816.

[40] PETITTO, S.C., LANGELL, M.A., "Surface composition and structure of Co_3O_4(110) and the effect of impurity segregation", *Journal of Vacuum Science & Technology. A, Vacuum, Surfaces, and Films*, v. 22, n. 4, pp. 1690–1696, Jul. 2004. doi: https://doi.org/10.1116/1.1763899.

[41] LAI, L., POTTS, J.R., ZHAN, D., *et al.*, "Exploration of the active center structure of nitrogen-doped graphene-based catalysts for oxygen reduction reaction", *Energy & Environmental Science*, v. 5, n. 7, pp. 7936, 2012. doi: https://doi.org/10.1039/c2ee21802j.

[42] LI, T., SHANG, D., GAO, S., *et al.*, "Two-dimensional material-based electrochemical sensors/biosensors for food safety and biomolecular detection", *Biosensors*, v. 12, n. 5, pp. 314, May. 2022. doi: https://doi.org/10.3390/bios12050314. PubMed PMID: 35624615.

[43] ZHAO, Z., ZHANG, J., WANG, W., *et al.*, "Synthesis and electrochemical properties of Co_3O_4-rGO/CNTs composites towards highly sensitive nitrite detection", *Applied Surface Science*, v. 485, pp. 274–282, Aug. 2019. doi: https://doi.org/10.1016/j.apsusc.2019.04.202.

[44] LIU, H., GUO, K., LV, J., *et al.*, "A novel nitrite biosensor based on the direct electrochemistry of horseradish peroxidase immobilized on porous Co_3O_4 nanosheets and reduced graphene oxide composite modified electrode", *Sensors and Actuators. B, Chemical*, v. 238, pp. 249–256, Jan. 2017. doi: https://doi.org/10.1016/j.snb.2016.07.073.

[45] LIN, X., RAO, S., YOU, Z., *et al.*, "Enhanced electrocatalytic activity of ZIF-67C/CuO-NiO composite for the sensoring of nitrite in food", *Journal of the Electrochemical Society*, v. 172, n. 10, pp. 107509, Oct. 2025. doi: https://doi.org/10.1149/1945-7111/ae13c4.